Journal of Alloys and Compounds 509 (2011) 4714–4721

Contents lists available at ScienceDirect

Journal of Alloys and Compounds

journal homepage: www.elsevier.com/locate/jallcom

Upconversion luminescence of $Yb^{3+}/Tb^{3+}/Er^{3+}$-doped fluorosilicate glass ceramics containing SrF_2 nanocrystals

Xvsheng Qiao, Xianping Fan*, Zheng Xue, Xuanhe Xu, Qun Luo

State Key Laboratory of Silicon Materials, Department of Materials Science and Engineering, Zhejiang University, Zheda Road 38#, Hangzhou 310027, PR China

ARTICLE INFO

Article history:
Received 17 September 2010
Received in revised form 17 January 2011
Accepted 18 January 2011
Available online 22 January 2011

Keywords:
Upconversion
$Yb^{3+}/Tb^{3+}/Er^{3+}$
Glass Ceramic
Nanocrystal

ABSTRACT

$Yb^{3+}/Tb^{3+}/Er^{3+}$-doped transparent alkaline earth fluorosilicate glass ceramics containing SrF_2 nanocrystals were prepared and their microstructures and spectroscopic properties were investigated. The formation of SrF_2 nanocrystals enriched with $Yb^{3+}/Tb^{3+}/Er^{3+}$ in the glass ceramics was confirmed by XRD, HRTEM and SAED. The glass ceramics exhibited intense upconversion luminescence behaviors, owing to efficient energy transfers from Yb^{3+} to Er^{3+} and Tb^{3+} and low phonon assistant non-radiative transition probabilities of excited Er^{3+} and Tb^{3+}. The upconversion could be enhanced significantly by increasing the annealing temperature and the luminescence color could be adjusted by varying the $Yb^{3+}/Tb^{3+}/Er^{3+}$ ratio. Upconversion of Er^{3+} could be described as sequential energy transfer from single Yb^{3+} to single Er^{3+}, while upconversion of Tb^{3+} described as cooperative energy transfer from double Yb^{3+} to single Tb^{3+}.

1. Introduction

Fluorosilicate glass ceramics have attracted much attention since they combine merits of both fluoride crystals with low phonon energy and silicate glasses with high thermal, mechanical and chemical stabilities. During the first decade of their emergence, great achievements had obtained about rare earth doped glass ceramics containing $Pb_xCd_{1-x}F_2$ or PbF_2 nanocrystals [1,2]. However, these above-mentioned materials involve poisonous lead and cadmium and thus cannot be widely used due to environmental concerns. Then, researchers developed fluorosilicate glass ceramics containing nanophase such as CaF_2, YF_3, Ba_2LaF_7 and $NaYF_4$ [3–6] crystalline dots to conquer the above problems. Due to the nano-size of the precipitated crystalline phase and the enrichment of rare earth ions into the nanocrystals, such glass ceramics presented enhanced luminescence behaviors [7–9], especially intense ultraviolet upconversion [10–12], and had high transparency. Those demonstrate them as potential candidate hosts of various optoelectronic devices [7,13–18]. In the present work, multi-color upconversion luminescence has been obtained by adjusting the $Yb^{3+}/Tb^{3+}/Er^{3+}$ doping ratio in the glass ceramic system of SiO_2–Al_2O_3–ZnF_2–SrF_2. The upconversion luminescence could be enhanced by increasing the annealing temperature. These give probabilities to apply such materials to the optoelectronic fields, such as color display, white light emitting and short wavelength solid state laser.

2. Experimental

The glass samples presented in this work had the following compositions (in mol%):

(1) $50SiO_2$–$10Al_2O_3$–$(16-x)$ ZnF_2–$20SrF_2$–$3.99YbF_3$–$0.01ErF_3$–$xTbF_3$ (x = 0.05, 0.1, 0.5, 1 and 2), named as G1#, G2#, G3#, G4# and G5#.

For comparison, the reference sample with the following composition (in mol%) were also involved in the XRD or spectral investigation:

(2) $50SiO_2$–$10Al_2O_3$–$20ZnF_2$–$20SrF_2$, named as GRef;
(3) $50SiO_2$–$10Al_2O_3$–$16ZnF_2$–$20SrF_2$–$4YbF_3$, named as GYb;
(4) $50SiO_2$–$10Al_2O_3$–$20ZnF_2$–$20SrF_2$–$3ErF_3$, named as GEr;
(5) $50SiO_2$–$10Al_2O_3$–$18ZnF_2$–$20SrF_2$–$2TbF_3$, named as GTb;
(6) $50SiO_2$–$10Al_2O_3$–$20ZnF_2$–$20SrF_2$–$3YbF_3$–$0.01ErF_3$, named as GYbEr;
(7) $50SiO_2$–$10Al_2O_3$–$20ZnF_2$–$20SrF_2$–$4YbF_3$–$2TbF_3$, named as GYbTb.

The glass samples were prepared by mixing high purity SiO_2, Al_2O_3, SrF_2, ZnF_2, YbF_3 and TbF_3 raw materials, melting them at 1400 °C for 45 min in a corundum crucible with an air atmosphere, pouring the melts onto a copper plate and pressing it by another copper plate immediately. According to DTA curves, such glass samples were annealed at 660 °C for 2 h to obtain a series of glass ceramics, named as GC1–5#, GCRef, GCYb, GCEr, GCTb, GCYbEr and GCYbTb, respectively. In order to investigate effects of the heat treat temperature on the properties of glass ceramics, another series of glass ceramics were also prepared by annealing G5# for 2 h at 600 °C (denoted as GC600), 620 °C (denoted as GC620), 640 °C (denoted as GC640), 660 °C (denoted as GC660), respectively.

DTA measurements for glass samples were carried out on a CDR-1 Differential Thermal Analyzer in ambient atmosphere with a heating rate of 10 °C/min to determine the glass transition temperature (T_g) and the crystallized peak temperature (T_c). All the glass and glass ceramics were polished on a UNIPOL-802 precision lapping/polishing machine to get optical quality for optical measurements. X-ray

* Corresponding author. Tel.: +86 571 87952334; fax: +86 571 87951234.
E-mail address: optglas@yahoo.com.cn (X. Fan).

0925-8388/$ – see front matter © 2011 Elsevier B.V. All rights reserved.
doi:10.1016/j.jallcom.2011.01.099

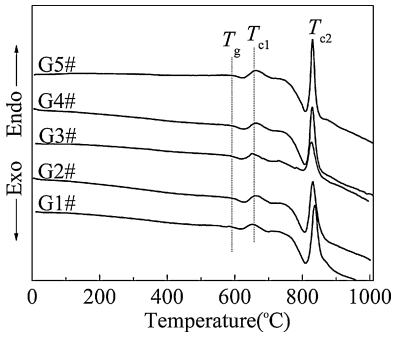

Fig. 1. DTA curve of the $50SiO_2–10Al_2O_3–(16-x)ZnF_2–20SrF_2–3.99YbF_3–0.01ErF_3–xTbF_3$ (x = 0.05, 0.1, 0.5, 1 and 2 in mol%) glass samples.

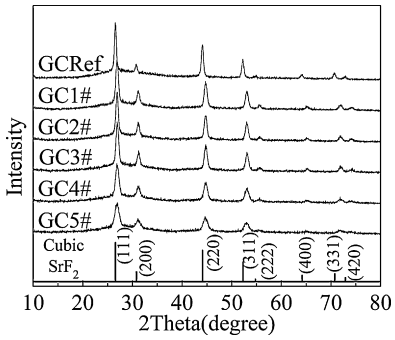

Fig. 3. XRD patterns of the $Yb^{3+}/Er^{3+}/Tb^{3+}$ tri-doped glass ceramic samples obtained by annealing the precursor glass samples for 2 h at 660 °C.

diffraction (XRD) measurements were performed on a XD-98 diffractometer with Cu-K_α radiation at 4°/min scanning rate and 0.02° step size. From XRD patterns, crystal sizes, d-spacing and their random errors were evaluated using Jade (Materials Data, Inc.). Transmission electron microscopy (TEM) and high resolution transmission electron microscopy (HRTEM) images were obtained on a JEOL JEM-2010HR microscopy. The analysis of HRTEM images was carried out with DigitalMicrograph (Gatan Inc.), and random errors were evaluated by sampling method. All steady luminescence measurements were performed on an Edinburgh FLS920P spectrometer at room temperature. Upconversion luminescence spectra were performed with excitation of 980 nm from a laser diode. Luminescence rising and decay curves were recorded with a HP546800B 100 MHz oscilloscope, using excitation of a light pulses of 940 nm LD. Spectra analyses were carried out with Origin (OriginLab Corporation) and random errors were also evaluated simultaneously. Systematical errors in the above measurements were minimized by calibrating instruments with standard samples.

3. Results and discussion

DTA curves (Fig. 1) shows that all glass samples have the similar glass transition temperatures (T_g) around 590 °C, the similar first crystallization peaks (T_{c1}) around 660 °C and the similar second crystallization peaks (T_{c2}) around 830 °C. According to the crystallization procedure experiments, the first crystallization peak T_{c1} can be ascribed to the precipitation of cubic SrF_2 crystals and the second crystallization peak T_{c2} to the bulk crystallization process of the whole matrix.

XRD patterns of the investigated glass and glass ceramics are depicted in Figs. 2–4. XRD patterns of the prestine glasses exhibit a broad diffraction band with a typical glassy feature and without any sharp diffraction peaks (except for G1#), while those of the glass ceramics have clear reflections. It is noted that G1# with weak crystalline XRD peaks was still into the glass series although a very small quantity of crystallization took place during casting the melt into a preheated mould. The crystalline phase of the glass ceramics could be easily assigned to the cubic SrF_2 phase. The size of the SrF_2 nanocrystals in the glass ceramics can be calculated by the Scherrer formula:

$$D_{h\,k\,l} = \frac{K\lambda}{\beta \cos\theta}, \quad (1)$$

where $D_{h\,k\,l}$ is the crystal size at the vertical direction of (h k l), λ is the wavelength of X-ray, θ is the angle of diffraction, β is the Full-Width Half-Maximum of the diffraction peak and the constant K = 0.90. The volume fraction of the crystalline phase (crystallinity) can also be estimated by the ratio of the integrated area of the diffraction peaks to the total area of the XRD pattern from 10° to 80° [19]. The calculated results have been shown in Table 1. For the glass ceramics with different Tb^{3+} concentration (GC1–GC5#), as shown in Fig. 3, the crystallinities are similar around 40%, but crystal size decreases from about 20 nm to 6.7 nm when Tb^{3+} content increasing from 0.05 mol% to 2 mol%. So Tb^{3+} dopant maybe restrain the growth of SrF_2 nanocrystals. For the glass ceramics annealed at different temperatures (GC600–660), as shown in Fig. 4, both crystallinity and crystal size increase with the heat treatment temperatures rising up. The crystallinity increases from 16.2% to 30.8%, and the crystal size increases from 2.1 to 6.7, when the heat treating temperature rises from 600 °C to 660 °C. It is remarked that for domain sizes of the order of few nanometers (e.g. 2.1 nm for the GC600 sample), surface effects becomes important and basic diffraction laws, like the Bragg's law, need to be reconsidered. Consequently, the average crystal size and the deviation are probably underestimated, because a second cause of broadening, such as the effects of stress, can also broaden XRD peaks. But the crystal sizes of GC600–660 were several nanometers and from the same method, so we still compare them to each other here.

X-ray diffraction angles of all the glass ceramics doped with rare earths moved to larger degree in comparison with the reference sample GCRef. From XRD peak positions, using Bragg diffraction formula, lattice interplanar spacings (d-spacing) can be determined.

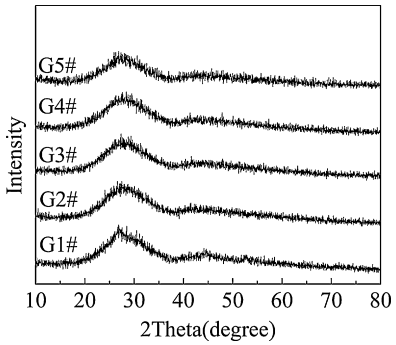

Fig. 2. XRD patterns of the $50SiO_2–10Al_2O_3–(16-x)ZnF_2–20SrF_2–3.99YbF_3–0.01ErF_3–xTbF_3$ (x = 0.05, 0.1, 0.5, 1 and 2 in mol%) glass samples.

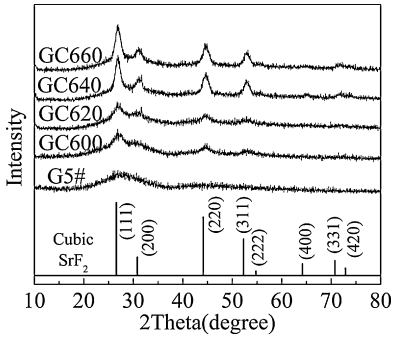

Fig. 4. XRD patterns of the $50SiO_2–10Al_2O_3–14ZnF_2–20SrF_2–3.99YbF_3–0.01ErF_3–2TbF_3$ glass and glass ceramic samples annealed for 2 h at different temperatures.

Table 1
Crystallinity and crystal size of the investigated glass and glass ceramics.

Sample name	Crystallinity (%)	Crystal size (nm)	Sample name	Crystallinity (%)	Crystal size (nm)
GCRef	33.0 ± 1.3	19.4 ± 0.1	GC600	16.2 ± 0.5	2.1 ± 0.1
GC1#	37.6 ± 0.9	17.9 ± 0.2	GC620	17.9 ± 0.7	3.5 ± 0.1
GC2#	39.8 ± 0.8	21.7 ± 0.3	GC640	30.4 ± 0.9	6.9 ± 0.1
GC3#	40.3 ± 0.7	17.5 ± 0.2	GC660	30.8 ± 0.9	6.7 ± 0.1
GC4#	37.9 ± 1.0	12.1 ± 0.1			
GC5#	30.8 ± 0.9	6.7 ± 0.1			

The calculated results of GC1# have been list in Table 1. The d-spacings of the precipitated SrF_2 (d_{XRD}) in GC1# are smaller than those of GCRef (d_{REF}) and the standard values (d_{STD}). It indicates the shrinkage of the SrF_2 crystalline lattice in GC1#. The lattice shrinkage is probably led by small Yb^{3+}/Tb^{3+}/Er^{3+} substituting large Sr^{2+} in SrF_2 crystalline phase, because Yb^{3+} (0.0868 nm), Tb^{3+} (0.0923 nm) and Er^{3+}(0.0890 nm) have smaller effective ionic radius than Sr^{2+} (0.118 nm) when coordinate number is six [20].

TEM images of the samples G5#, GC5# and GC1# are shown in Fig. 5(a)–(c), where inset graphs are selected area electron diffraction (SAED) patterns. Glass sample G5# presents a uniform image contrast under TEM, while GC5# and GC1# present many second circular nanophases with enhanced diffraction contrast embedded in gray background. Undoubtedly, the gray background is glass phase, and the circular spots are the precipitated SrF_2 nanocrystals. The inset SAED patterns of G5# shows only one centered diffractive spot, which reveals the amorphous nature of G5#, while those of GC5# and GC1# exhibit clear lattice diffractive rings. The SAED patterns containing Bragg intensities on concentric circles indicate random orientation of the nanoparticles inside the matrix material and correspond to the (1 1 1), (2 0 0) and (2 2 0) planes of the SrF_2 nanocrystals with the ring radius increasing. The diffractive pattern of GC1# is more clearly observable than GC5#. It indicates GC1# contains more well-grown nanocrystals (sized 10–20 nm) than GC5# (sized < 5 nm). Those agree well with the above XRD calculated results and reveal crystal size decreasing with Tb^{3+} content increasing. Due to much smaller size of precipitated SrF_2 nanocrystals than the wavelength of the visible light, such glass ceramics containing SrF_2 nanocrystals still keep high transparency.

The real structure of the precipitated SrF_2 nanocrystals in the glass matrix can be studied with high resolution transmission electron microscope (HRTEM). The magnified HRTEM image of a single SrF_2 nanocrystal in GC1# is shown in Fig. 6(a), and the corresponding Fast Fourier Transform (FFT) is shown in Fig. 6(b). The calculated d-spacings from HRTEM lattice image and SAED patterns has been summarized in Table 2. Here d_{HRTEM} agrees well with d_{XRD}, while d_{SAED} appears the slight deviation due to the camera systematical errors. Similar with d_{XRD} results, both of d_{SAED} and d_{HRTEM} are much smaller than the standard value (d_{STD}). It indicates a number of Yb^{3+}/Tb^{3+}/Er^{3+} ions, with smaller ionic radii than Sr^{2+}, have occupied some Sr^{2+} sites and hence entered into the precipitated SrF_2 crystalline phase. Upon the above phase and microstructure evolution from the precursor glass to the glass ceramics, one can expect the luminescence behavior difference between the glass and the glass ceramics, which can be revealed by the following spectral analysis.

The spectra of single- and co-doped reference samples are shown in Fig. 7(a). One can clearly observe the emission band assigned to single doped Yb^{3+}, Er^{3+} or Tb^{3+}: (1) sample GCYb emits blue upconversion luminescence. The 479 nm Yb^{3+} upconversion can be assigned to the cooperative upconversion process of Yb^{3+}: $^2F_{7/2} + {}^2F_{7/2} \rightarrow {}^2F_{5/2} + {}^2F_{5/2}$, while the other upconversion peaks of GCYb, respectively at 408 nm, 540 nm and 650 nm, can be ascribed to the luminescence of Er^{3+} involved as impurities with concentration less than 100 ppm. Generally, Yb^{3+} ion has only one excited state $^2F_{5/2}$, locating about 10^{-4} cm^{-1} above the ground stated $^2F_{7/2}$, so that it cannot fluorescence in the visible region. But the cooperative upconversion luminescences of Yb^{3+} in visible region have been reported in many Refs. [21–27]. The photon energy of 479 nm-peaks is exactly twice the energy of the normal Yb^{3+} luminescence due to the $^2F_{7/2} \rightarrow {}^2F_{5/2}$ transition, locating from 900 nm to 1100 nm, so it can be assigned to the cooperative upconversion luminescence of the Yb^{3+}. Besides, a weak peak at 462 nm and a strong peak at 479 nm are observed clearly for the cooperative luminescence of the Yb^{3+} ions here. It indicates there are several stark levels of the ground and excited states. This may be due to by the coordination of Yb^{3+} with the precipitated nanocrystal phase of SrF_2. (2) Sample GCEr presents two intense upconversion emission bands centered at 544 nm and 660 nm with two weak emission bands around 408 nm and 522 nm. Such emission bands can be assigned to $^2H_{9/2} \rightarrow {}^4I_{15/2}$ (408 nm), $^2H_{11/2} \rightarrow {}^4I_{15/2}$ (522 nm), $^4S_{3/2} \rightarrow {}^4I_{15/2}$ (544 nm), $^4F_{9/2} \rightarrow {}^4I_{15/2}$ (660 nm) transitions of Er^{3+}. (3) Sample GCTb presents no upconversion luminescence with 980 nm LD excitation, so the luminescence spectrum was obtained with 235 nm Xe-lamp excitation. The emission bands of GCTb can be assigned to $^5D_3$, $^5G_6 \rightarrow {}^7F_6$ (381 nm), $^5D_3$, $^5G_6 \rightarrow {}^7F_5$ (415 nm), $^5D_3$,$^5G_6 \rightarrow {}^7F_4$ (439 nm), $^5D_4 \rightarrow {}^7F_6$ (489 nm), $^5D_4 \rightarrow {}^7F_5$ (543 nm), $^5D_4 \rightarrow {}^7F_4$ (585 nm) and $^5D_4 \rightarrow {}^7F_3$ (620 nm) transitions of Tb^{3+}.

Different from the single doped, for Yb^{3+}–Er^{3+} codoped or Yb^{3+}–Tb^{3+} codoped, some upconversion bands of Er^{3+} or Tb^{3+} are enhanced so much that the co-doped samples present intense upconversion luminescence even in ultraviolet region, as the spectra of GCYbEr and GCYbTb in Fig. 7(a) show. Because both Yb^{3+} and Er^{3+} ions have absorption band around 980 nm and the absorption cross section of Yb^{3+} ions is much larger than that of Er^{3+} ions, the energy transfer from Yb^{3+}: $^2F_{5/2}$ to Er^{3+}: $^4I_{11/2}$ state is efficient in Yb^{3+}–Er^{3+} codoped systems. Accordingly, the 408 nm upconversion peak of GCYbEr is several ten times as strong as that of GCEr. A weak

Table 2
Standard interplanar spacing of the cubic SrF_2 crystalline phase and calculated interplanar spacing of the precipitated SrF_2 crystalline phase in sample GC1#.

Lattice plane	d_{STD}[a] (Å)	d_{REF}[b] (Å)	d_{XRD}[c] (Å)	d_{SAED}[d] (Å)	d_{HRTEM}[e] (Å)
(1 1 1)	3.3520	3.3535 ± 0.0022	3.3152 ± 0.0009	3.3077 ± 0.0045	3.3170 ± 0.0037
(2 0 0)	2.9000	2.9027 ± 0.0043	2.8680 ± 0.0012	2.8671 ± 0.0129	2.8685 ± 0.0114
(2 2 0)	2.0508	2.0526 ± 0.0012	2.0252 ± 0.0004	2.0238 ± 0.0066	2.0279 ± 0.0043

[a] d_{STD}: from the standard PDF card(# 06-0262).
[b] d_{REF}: from the XRD peak positions of GCRef.
[c] d_{XRD}: from the XRD peak positions of GC1#.
[d] d_{SAED}: from the selected area electron diffraction patterns of GC1#.
[e] d_{TEM}: from the HRTEM image of GC1#.

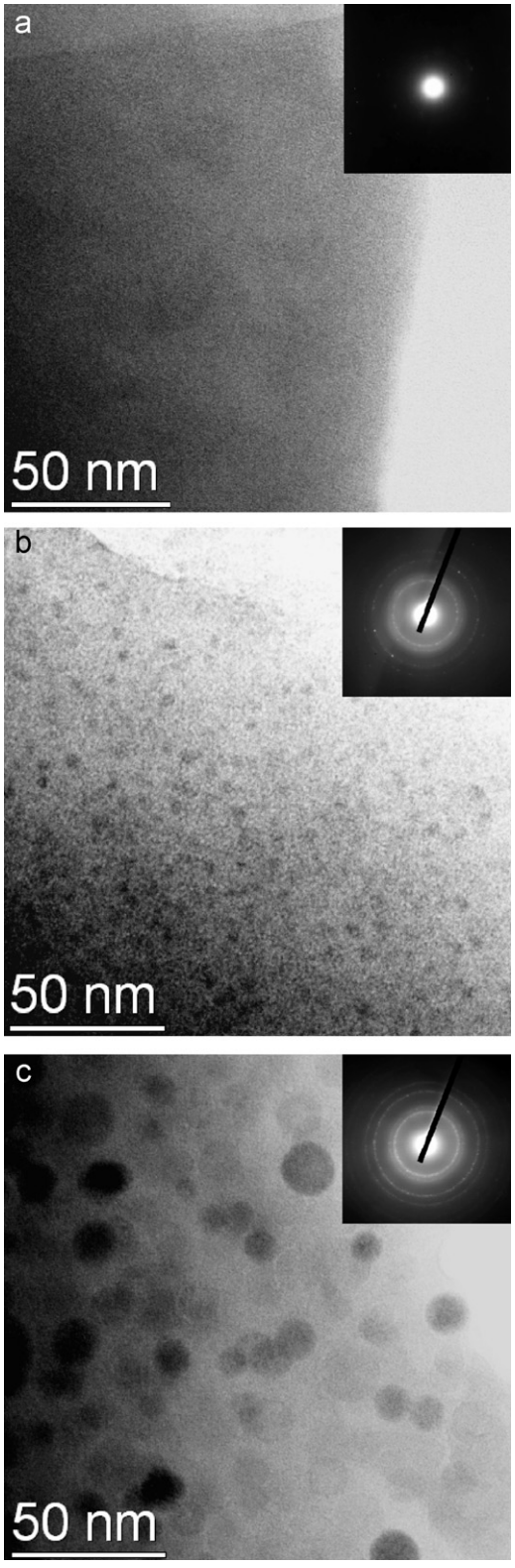

Fig. 5. TEM images of the samples G5# (a), GC5# (b) and GC1# (c) (inset graphs: selected area electron diffraction patterns.).

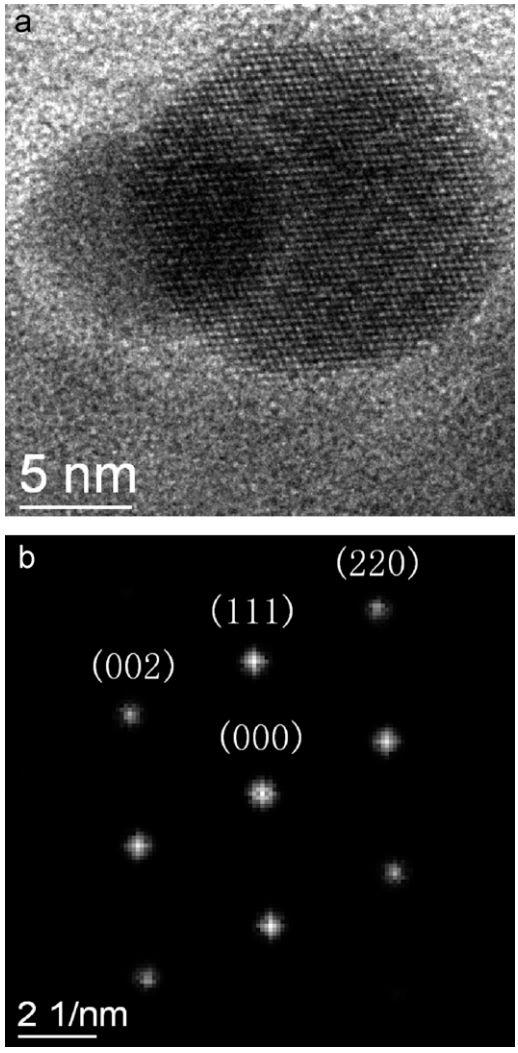

Fig. 6. HRTEM image (a) of the domain centered with one nanocrystal in the sample GC1#, and the corresponding reciprocal diffraction lattice pattern (b) obtained by Fast Fourier Transform (FFT).

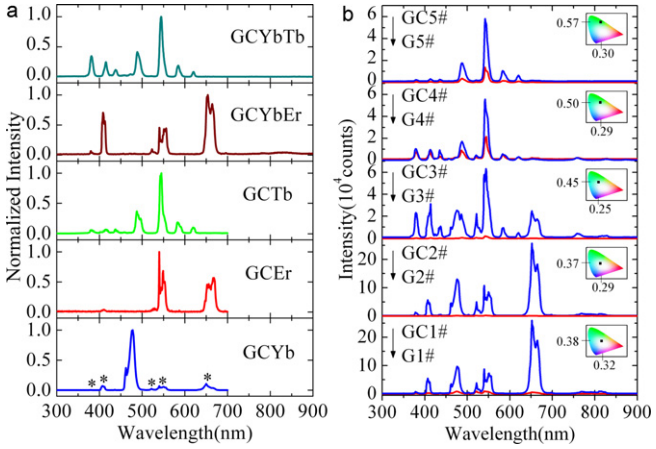

Fig. 7. Upconversion luminescence spectra (exciting with a 300 mW LD at 980 nm) of the single- and co-doped reference samples (a) and the $Yb^{3+}/Er^{3+}/Tb^{3+}$ tri-doped samples (b). Inset shows CIE coordinate of the corresponding glass ceramics.

upconversion emission peak of GCYbEr also appears at 380 nm (Er^{3+}: $^4G_{11/2} \rightarrow {}^4I_{15/2}$), which cannot be observed from that of GCEr. Furthermore, the spectrum of GCYbEr consists of blue, green and red emission bands which are three elements of white light. So GCYbEr can be a candidate for white light emission. However, CIE (the

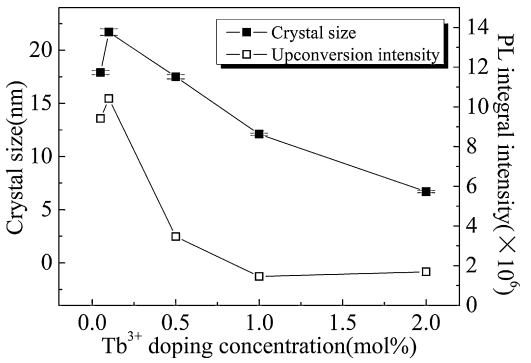

Fig. 8. Dependence of crystal size (left axis) and upconversion luminescence intensities (right axis) on Tb^{3+} doping concentration of the $Yb^{3+}/Er^{3+}/Tb^{3+}$ tri-doped glass ceramic samples annealed at 660 °C.

Commission International de l'Eclairage) chromaticity coordinates for GCYbEr is (0.40, 0.51), which deviating from that of pure white light (0.33, 0.33). The color rendering index of Yb^{3+}–Er^{3+} codoped systems might be poor due to the lack of blue and green emission. GCYbTb presents strong near ultraviolet to blue upconversion luminescence centered at 381 nm, 415 nm and 439 nm, as shown in Fig. 7(a), which is complementary to the upconversion luminescent color of GCYbEr and derived from the cooperative energy transfer between Yb^{3+} pairs and Tb^{3+}. Therefore, tri-doped with Yb^{3+}–Er^{3+}–Tb^{3+}, the present fluorosilicate glass ceramics can be expected to emit white upconversion luminescence.

Fig. 7(b) shows the upconversion spectra of the Yb^{3+}–Er^{3+}–Tb^{3+} tri-doped glass and glass ceramics and insets shows the CIE coordinate of the glass ceramics. Referring to the single doped samples, one can find that the upconversion spectra of 1–2# glass and glass ceramics compose of emission bands of Yb^{3+} and Er^{3+}, those of 3–4# glass and glass ceramics compose of emission bands of Yb^{3+}, Er^{3+} and Tb^{3+}, and those of 5# glass and glass ceramics only compose of emission bands of Tb^{3+}. Similar with the single-Yb^{3+}-ion luminescence involving several stark levels of the ground and excited states, a weak peak at 462 nm and a strong peak at 479 nm are observed clearly for the cooperative luminescence of the Yb^{3+} ions here, since it also consists of such stark-level-transitions, indicating the entrance of Yb^{3+} ions into the precipitated nanocrystals

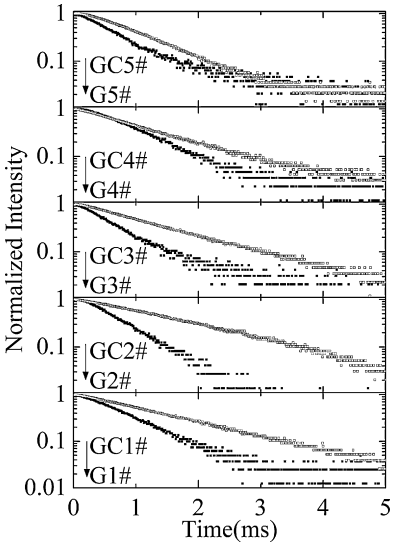

Fig. 9. 977 nm luminescence decay curves (exciting at 940 nm with a pulsed LD) of the $Yb^{3+}/Er^{3+}/Tb^{3+}$ tri-doped glass ceramic samples annealed at 660 °C and the precursor glass samples.

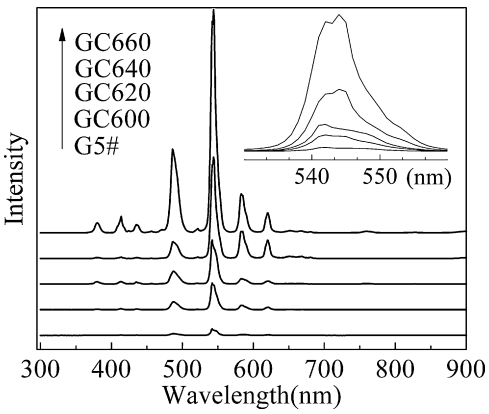

Fig. 10. Upconversion luminescence spectra (exciting with a 300 mW LD at 980 nm) of the $50SiO_2$–$10Al_2O_3$–$14ZnF_2$–$20SrF_2$–$3.99YbF_3$–$0.01ErF_3$–$2TbF_3$ glass and glass ceramic samples annealed for 2 h at different temperatures. The inset graph shows predominant emission peaks of the glass ceramics around 542 nm.

of SrF_2. The energy transfer from Yb^{3+} to Tb^{3+} cannot take place simultaneously with Yb^{3+} to Er^{3+} when the doping level of Tb^{3+} is low (samples 1–2#), because the cooperative energy transfer from Yb^{3+} to Tb^{3+} is less effective than the common energy transfer upconversion (such as APTE) by 4–5 orders of magnitude [28]. Such cooperative energy transfer demands much short ionic distance (<5 Å), therefore take places only when the doping level is relatively high [28–31]. The emission bands of Tb^{3+} cannot be detected until the Tb^{3+} concentration ≥5 mol% (samples 3–5#). However, the Er^{3+} upconversion is quenched down and disappears with the Tb^{3+} concentration increasing, which is probably led by the energy transfer from Er^{3+} to Tb^{3+} at the high Tb^{3+} concentration. The possible energy transfer mechanism is Er^{3+}: $^4F_{7/2}$ +Tb^{3+}: $^7F_6 \rightarrow Er^{3+}$: $^4I_{15/2}$ +Tb^{3+}: $^5D_4$, since the energy gap of both Tb^{3+}: $^7F_6 \rightarrow {}^5D_4$ and Er^{3+}: $^4F_{7/2} \rightarrow {}^4I_{15/2}$ is nearly the same and also nearly twice the energy of Yb^{3+}: $^2F_{7/2} \rightarrow {}^2F_{5/2}$. Additionally, with the Tb^{3+} concentration increasing, sample 5# present weaker near ultraviolet upconversion than sample 4#. That may be also led by the luminescence quenching effect of Tb^{3+}.

All the glass ceramics present much stronger upconversion luminescence than the precursor glasses. It may be led by the cluster or enrichment effect of rare earth ions in the precipitated SrF_2 nanophase and by the much lower phonon energy of the SrF_2 nanophase than that of the glass matrix. On the one hand, both the cooperative and the common energy transfer upconversion

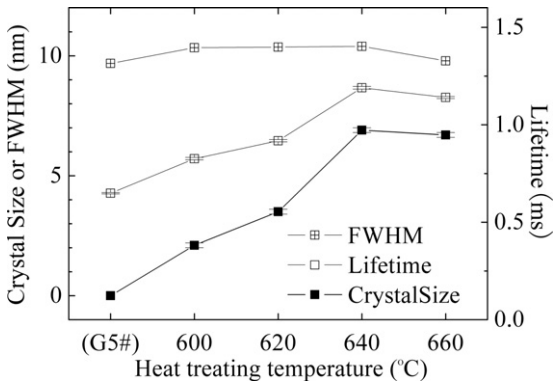

Fig. 11. Dependence of the FWHM (left axis) of the Tb^{3+}: $^5D_4 \rightarrow {}^7F_5$ upconversion emission around 542 nm, the lifetime (right axis) of the Yb^{3+}: $^2F_{7/2} \rightarrow {}^2F_{5/2}$ emission around 980 nm and the crystal size (left axis) of the precipitated SrF_2 nanophase on the heat treating temperature of the $50SiO_2$–$10Al_2O_3$–$14ZnF_2$–$20SrF_2$–$3.99YbF_3$–$0.01ErF_3$–$2TbF_3$ glass ceramic samples.

Table 3
Lifetimes (τ) of Yb^{3+}: $^2F_{5/2}$ state in the investigated glasses and glass ceramics.

Sample name	τ (ms)	Sample name	τ (ms)	Sample name	τ (ms)
G1#	0.769 ± 0.004	GC1#	1.410 ± 0.004	G5#	0.649 ± 0.004
G2#	0.660 ± 0.005	GC2#	1.580 ± 0.006	GC600	0.826 ± 0.006
G3#	0.641 ± 0.004	GC3#	1.250 ± 0.003	GC620	0.918 ± 0.006
G4#	0.873 ± 0.005	GC4#	1.110 ± 0.003	GC640	1.190 ± 0.007
G5#	0.649 ± 0.004	GC5#	1.140 ± 0.005	GC660	1.140 ± 0.005

depend on inter-ionic distances (it relies upon Coulomb interaction between ions) [32]. Theoretically, the radiative transition probability from energy transfer (W_{ET}), has the following relationship [33] with the distances between the donor and acceptor ions (r_{D-A}):

$$W_{ET} \propto \frac{1}{r_{D-A}^6} \quad (2)$$

As Yb^{3+}, Tb^{3+} and Er^{3+} ions in the glass ceramics have been enriched in SrF_2 nanocrystals, local higher rare earth concentration and closer ionic distance in the glass ceramics could be obtained and more efficient energy transfer from Yb^{3+} to Er^{3+} or Tb^{3+} could be expected for the glass ceramics. On the other hand, the upconversion luminescence of $Er^{3+}$and Tb^{3+} ions in the glass ceramics can also be enhanced by lower multi-phonon decay rate in the precipitated SrF_2 nanocrystals. Multi-phonon non-radiative processes would cut down the luminescence quantum efficiency significantly. For a given energy gap, the most critical factor affecting the multi-phonon relaxation is the maximum energy, $\hbar\omega_{max}$, of the host lattice phonons [34,35]. The lower the maximum phonon energy is, the smaller the multi-phonon non-radiative decay rate will be. Due to much smaller $\hbar\omega_{max}$ of SrF_2 (about 300 cm^{-1}) [36] than that of the silicate glass matrix (about 1100 cm^{-1}), the multi-phonon non-radiative transition probabilities of Tb^{3+} or Er^{3+} is much lower in the SrF_2 nanocrystals than that in the glass matrix. Accordingly, upconversion luminescences of all the glass ceramics are stronger than the precursor glass.

It is interesting that the upconversion intensity and the crystal size vary synchronously with the Tb^{3+} concentration (as Fig. 8 shows), which reveals the effect of the crystal field on the upconversion luminescence. Upconversion can be strengthened by a strong fluoride coordination environment, corresponding to a large crystal size. Firstly, all the glass ceramics present much stronger upconversion luminescence than the precursor glass because of the lower phonon energy of the precipitated SrF_2 nanocrystals; secondly, when Tb^{3+}doping level is lower, upconversion luminescences of GC1–2# are predominant by Yb^{3+}–Er^{3+} and influenced by the crystal size of SrF_2 nanocrystals; thirdly, as emission bands of Tb^{3+} appear and those of Er^{3+} disappear, upconversion luminescence of GC3–4# are weaken down subsequently because the energy transfer of Yb^{3+}–Tb^{3+} is less efficient than Yb^{3+}–Er^{3+}; finally, GC4–5# presented upconversion luminescence only derived from Yb^{3+}–Tb^{3+}, and those are dominated by the Tb^{3+} concentration, where the green upconversion intensity of GC5# > GC4# while the near ultraviolet upconversion intensity of GC5# < GC4#. Here different glass ceramic samples get intense upconversion luminescence with different colors (see insets in Fig. 7b), deriving from emission of Yb^{3+}, Er^{3+} and Tb^{3+}. Then, if mixing well with those emission bands, one can adjust the luminescence color as need.

From the near infrared luminescence decay curves, as shown in Fig. 9 (monitoring at 1020 nm; exciting at 940 nm), lifetimes of the excited state can be evaluated. Decay curves of these samples comply with single exponential laws, then luminescence lifetimes, τ, can be calculated by evaluation of decay curves $I(t) = A \times \exp(-t/\tau)$, as list in Table 3. Since both radiative and non-radiative processes

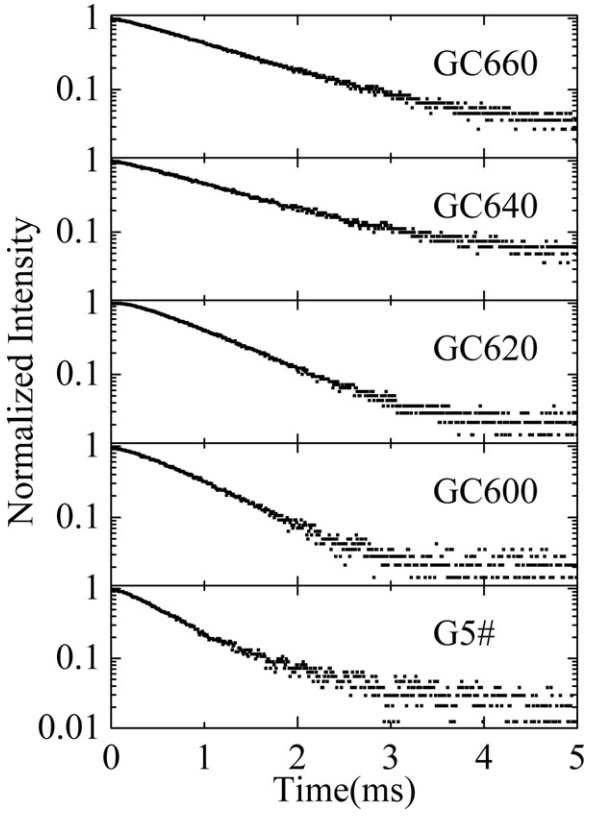

Fig. 12. 977 nm luminescence decay curves (exciting at 940 nm with a pulsed LD) of the $50SiO_2$–$10Al_2O_3$–$14ZnF_2$–$20SrF_2$–$3.99YbF_3$–$0.01ErF_3$–$2TbF_3$ glass and glass ceramic samples annealed for 2 h at different temperatures.

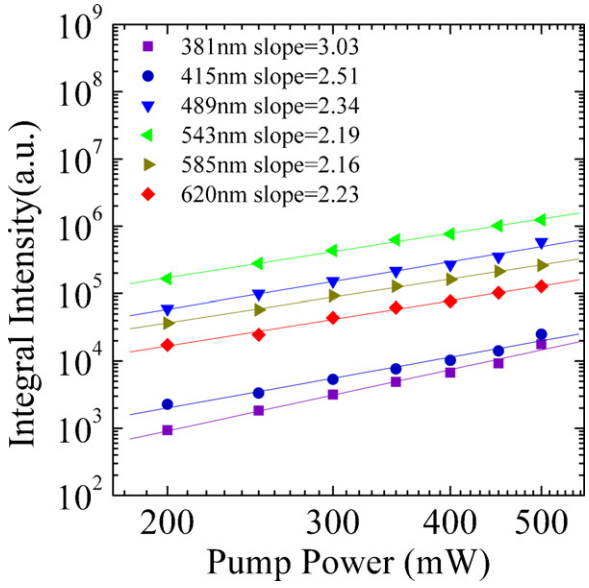

Fig. 13. Dependence of upconversion luminescence integral intensity of the $50SiO_2$–$10Al_2O_3$–$14ZnF_2$–$20SrF_2$–$3.99YbF_3$–$0.01ErF_3$–$2TbF_3$ glass ceramic (GC5#) on the LD pumping power (both axes are logarithmic).

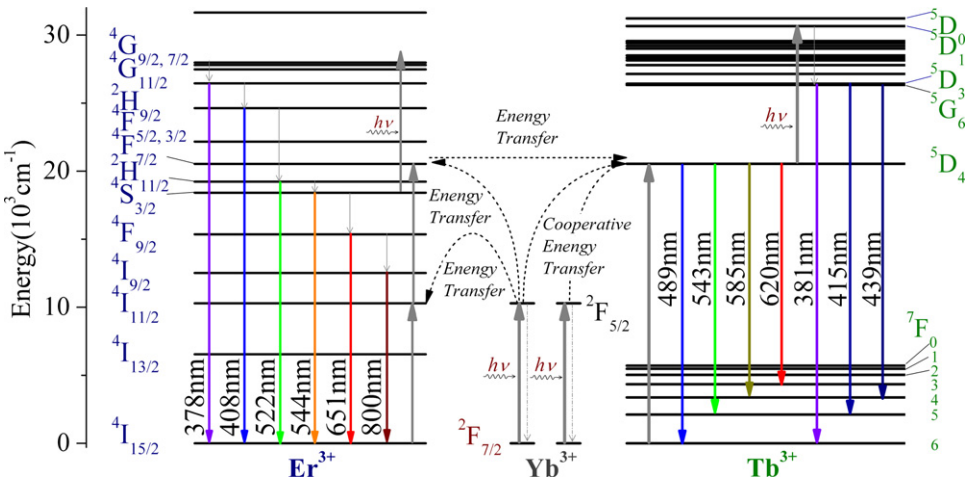

Fig. 14. Simplified energy level diagrams of Er^{3+}, Yb^{3+} and Tb^{3+} ions, and possible upconversion luminescence mechanisms under the 980 nm LD excitation.

operate to relax an excited state in the usual case, we can express the total luminescence lifetime of the excited state as:

$$\tau^{-1} = W_R + W_{NR} \quad (3)$$

where W_R is the radiative rate and W_{NR} is the sum of the rates of the various nonradiative processes. The nonradiative processes mainly include the phonon-assistant nonradiative process and energy transfer processes. With the Tb^{3+} concentration increasing, because much more energy transfer processes take place from Yb^{3+} to Tb^{3+} under 980 nm LD pumping, the Yb^{3+}: $^2F_{5/2}$ lifetime appears decreasing tendency (see Table 3). In addition, all the glass ceramics present longer Yb^{3+}: $^2F_{5/2}$ lifetimes than the precursor glass. This may be due to different coordination environment of Yb^{3+} in the glass ceramics and the precursor glass. Some references [37–39] have reported Yb^{3+} ions had longer excited state lifetimes in fluoride hosts than those in silicates. Here Yb^{3+} ions are mainly coordinated with Si–O matrix in the precursor glasses, while enriched into the precipitated SrF_2 nanocrystallline phase in the glass ceramics. Glass ceramic samples thus have much longer Yb^{3+} excited state lifetimes.

To investigate effects of heat treat temperature on spectroscopic properties of glass ceramics, glass ceramics were also prepared by annealing G5# for 2 h at different temperatures and their visible upconversion luminescence spectra were shown in Fig. 10. With the heat treating temperature rising up, the glass ceramics subsequently present stronger upconversion luminescence owing to the enrichment of rare earth ions in the precipitated SrF_2 phase with low phonon energy. Each emission spectrum appears similar in shape and each emission band is easily assigned to the same transitions of Tb^{3+} in GC5#, but the relative intensities for the specific wavelength 544–542 nm are enhanced as the inset graph of Fig. 10 showed. In this means, the emission band of Tb^{3+}: $^5D_4 \rightarrow {}^7F_5$ is broadened, which can be evaluated by the spectral broadening (FWHM). In a crystalline or glassy host, the spectral broadening is influenced by the strength of the ligand field around rare earth dopant ions. The spectral broadening increases with the strength of electric dipoles [40,41], which is proportional to the radiative rate (W). Fig. 11 shows the FWHM of the Tb^{3+}: $^5D_4 \rightarrow {}^7F_5$ emission, the lifetimes of the Yb^{3+}: $^2F_{7/2} \rightarrow {}^2F_{5/2}$ transition and the crystal size of the precipitated SrF_2 nanophase increase monotonically with the heat treating temperatures. It confirms that the crystallization (crystal size) is broadening the emission band width (FWHM) and then enhancing the magnitude of electric dipole eventually. The lifetimes of the Yb^{3+}: $^2F_{7/2} \rightarrow {}^2F_{5/2}$ transitions are calculated from the decay curves of near infrared luminescence around 980 nm, as shown in Figs. 12 and 13 and Table 3. From the radiative rate theory [40,41], the lifetime (τ) is inversely proportional to the radiative rate, so the spectral broadening (FWHM) is inversely related with the lifetime, which can also be expressed by the uncertainty principle on energy differential (ΔE) and time differential ($\Delta\tau$):

$$\Delta E^{\bullet}\Delta\tau \geq \frac{\hbar}{2} \quad (4)$$

However, from Fig. 11, it is evident that the standard relationship for the lifetime and FWHM, as described by the uncertainty principle above, is not followed. We believe this is led by the exceptional microstructure of the glass ceramics. Those are: (1) nano-SrF_2 crystals were embedded in the glass matrix, so the ligand field change is limited within nano range; (2) a part of rare earth dopant ions still remain in the glassy phase and serve for the emission bandwidth without large loss. Therefore, with the heat treating temperature rising up and the precipitated SrF_2 nanocrystals grow up, the upconversion luminescence, the spectral broadening, and the excited lifetime increase monotonically.

The dependence of luminescence intensity on pump-power is essential to understand excitation mechanisms in upconversion materials. In the simplest upconversion processes, it is generally assumed that the following relation existed between the emission intensity I_{em} and the IR excitation intensity P:

$$I_{em} \propto P^n \quad (5)$$

where the order n is the number of pump photons required exciting the emitting state, which is indicated by the slope of the luminescence intensity versus pump power in double-logarithmic [42]. However, a realistic upconversion system will exhibit an intensity-versus-power dependence, which is less than P^n. It is led by the increasing competition between linear decay and upconversion deriving from higher pump power, which will deplete excited electrons of the intermediate excited states, and, consequently, result in a significantly reduced slope. Fig. 13 shows the dependence of the upconversion luminescence intensity of GC660 on the LD pumping power. For 381 nm, 415 nm, 489 nm, 543 nm, 585 nm and 620 nm upconversion of Tb^{3+}, the n values is 3.03, 2.51, 2.34, 2.19, 2.16 and 2.23, respectively. According to the energy diagrams of Yb^{3+} and Tb^{3+}, as shown in Fig. 14, one can reasonably believe that the 381 nm, 415 nm and 489 nm Tb^{3+}-upconversion of GC660 are related with 3-photon process, while the other Tb^{3+}-upconversions are mainly 2-photon process partially mixed with 3-photon process. Fig. 14 also illustrates the above Yb^{3+}–Tb^{3+} upconversion luminescence mechanisms. Pumping at 980 nm, quantities of Yb^{3+} are excited to the excited state: $^2F_{7/2}$, then efficient cooperative energy transfer take place from two Yb^{3+} ions to their neighbor

Tb^{3+} ions, and the excited state $^5D_4$ of Tb^{3+} is populated largely. Furthermore, by absorbing another 980 nm photon via excited state absorption (ESA) or energy transfer (ET) from another excited Yb^{3+}, electrons at Tb^{3+}: $^5D_4$ can still be excited to upper energy level Tb^{3+}: $^5D_1$. Assisting with multiphonon relaxations, energy levels lower than Tb^{3+}: $^5D_1$ are populated. Eventually, radiative transitions of Tb^{3+}: $^5D_3$, $^5G_6 \rightarrow {}^7D_J$ (J = 6, 5, 4) emit 381 nm, 415 nm and 439 nm photons, and radiative transitions of Tb^{3+}: $^5D_4 \rightarrow {}^7D_J$ (J = 6, 5, 4, 3) emit 489 nm, 543 nm, 585 nm and 620 nm photons. Since the Tb^{3+}: $^5D_4$ state can be populated by both energy transfer from Yb^{3+} and multiphonon relaxation from upper levels, the 489 nm, 543 nm, 585 nm and 620 nm upconversions appear characteristics of mixing with 2- and 3-phonton processes. Besides, energy transfer exist between Yb^{3+} and Er^{3+} in the present samples, which have the similar mechanisms with the Yb^{3+}/Er^{3+} codoped system [43]. For upconversion of Er^{3+} in GC1–3#, both 378 nm and 408 nm could be described by 3-phonton processes, while 522 nm, 544 nm, 651 nm and 800 nm could be described by 2-phonton processes.

4. Conclusions

The $Yb^{3+}/Tb^{3+}/Er^{3+}$-doped transparent glass ceramics containing SrF_2 nanocrystals were prepared by heat treating the precursor fluorosilicate glass. The precipitated crystal size increased with Tb^{3+} doping level decreasing or heat treating temperature rising up. Owing to the enrichment of rare earth into the SrF_2 nanocrystalline phase, the glass ceramics could emit much more intense upconversion luminescence than the precursor glasses. This is indeed ascribed to efficient energy transfers from Yb^{3+} to Er^{3+} and Tb^{3+} and low phonon assistant non-radiative transition probability for excited state Er^{3+} and Tb^{3+} in the glass ceramics. With the heat treating temperature increasing, the upconversion luminescence, the spectral broadening, and the excited lifetime increase monotonically. Upconversion of Er^{3+} could be described as 2- or 3-photon processes mainly including sequential energy transfer from single Yb^{3+} to single Er^{3+}, while upconversion of Tb^{3+} described as 2- or 3-photon processes mainly including cooperative energy transfer from double Yb^{3+} to single Tb^{3+}. And multicolor upconversion luminescence could be obtained by adjusting the $Yb^{3+}/Tb^{3+}/Er^{3+}$ doping ratio. It suggested the present glass ceramics had potential application in the fields of color display and white light emitting.

Acknowledgements

The authors gratefully acknowledge support for this research from the National Nature Science Foundation of China (No. 50902120), the Research Fund of the Doctoral Program of Higher Education of China (20070335012) and Program for Changjiang Scholars and Innovative Research Team in University.

References

[1] Y. Wang, J. Ohwaki, Appl. Phys. Lett. 63 (1993) 3268.
[2] Y. Kawamoto, R. Kanno, J. Qiu, J. Mater. Sci. 33 (1998) 63.
[3] Y. Liu, B. Zhu, Y. Dai, X.S. Qiao, S. Ye, Y. Teng, Q.T. Guo, H.L. Ma, X.P. Fan, J.R. Qiu, Opt. Lett. 34 (2009) 3433.
[4] F. Liu, E. Ma, D. Chen, Y. Wang, Y. Yu, P. Huang, J. Alloys Compd. 467 (2009) 317.
[5] X.P. Fan, J. Wang, X.S. Qiao, M.Q. Wang, J.L. Adam, X.H. Zhang, J. Phys. Chem. B 110 (2006) 5950.
[6] H. Ping, D. Chen, Y. Yu, Y. Wang, J. Alloys Compd. 490 (2010) 74.
[7] J. Mendez-Ramos, V.K. Tikhomirov, V.D. Rodriguez, D. Furniss, J. Alloys Compd. 440 (2007) 328.
[8] J. Xie, Q. Zhang, Y. Zhuang, X. Liu, M. Guan, B. Zhu, R. Yang, J. Qiu, J. Alloys Compd. 509 (2011) 3032.
[9] A. Sarakovskis, J. Grube, G. Doke, M. Springis, Opt. Mater. 32 (2010) 832.
[10] D.Q. Chen, Y.S. Wang, Y.L. Yu, P. Huang, Appl. Phys. Lett. 91 (2007) 051920.
[11] Z.C. Duan, J.J. Zhang, W.D. Xiang, H.T. Sun, L.L. Hu, Mater. Lett. 61 (2007) 2200.
[12] X. Qiao, X. Fan, Z. Xue, X. Xu, J. Non-Cryst. Solids 357 (2011) 83.
[13] V. Scarnera, B. Richards, A. Jha, G. Jose, C. Stacey, Opt. Mater. 33 (2010) 159.
[14] J. Qiu, Chem. Rec. 4 (2004) 50–58.
[15] F. Yang, G. Chen, Z. You, C. Tu, Mater. Lett. 64 (2010) 824.
[16] T. Honma, M. Kanno, T. Komatsu, Mater. Sci. Eng. B: Adv. 171 (2010) 25.
[17] A. Santana-Alonsoa, J. Méndez-Ramosb, A.C. Yanesa, J. del-Castilloa, V.D. Rodríguezb, Mater. Chem. Phys. 124 (2010) 699.
[18] X. Sun, S. Huang, Nucl. Instrum. Meth. A 621 (2010) 322.
[19] B.He Bob, Two-dimensional X-ray Diffraction, John Wiley & Sons, New York, 2009, pp. 369–370.
[20] R.D. Shannon, Acta Crystallogr. A 32 (1976) 17.
[21] V.D. Cacho, L.R.P. Kassab, S.L. Oliveira, R.D. Mansano, P. Verdonck, Thin Solid Films 515 (2006) 764.
[22] E. Montoya, O. Espeso, L.E. Baus, J. Lumin. 87–89 (2000) 1036.
[23] P. Goldner, F. Pell, D. Meichenin, F. Auzel, J. Lumin. 71 (1997) 137.
[24] P. Goldner, F. Pell, F. Auzel, J. Lumin. 72–74 (1997) 901.
[25] E. Nakazawa, S. Shionoya, Phys. Rev. Lett. 25 (1970) 1710.
[26] D. Chen, Y. Yu, P. Huang, F. Weng, H. Lin, Y. Wang, Appl. Phys. Lett. 94 (2009) 041909.
[27] D. Deng, S. Xu, R. Bao, S. Zhao, B. Wang, H. Wang, H. Ju, J. Phys. D: Appl. Phys. 42 (2009) 105111.
[28] F. Auzel, Chem. Rev. 104 (2003) 139.
[29] F. Auzel, J. Lumin. 45 (1990) 341.
[30] P. Goldner, F. Pelle, F. Auzel, J. Lumin. 72–74 (1997) 901.
[31] P. Goldner, F. Pelle, D. Meichenin, F. Auzel, J. Lumin. 71 (1997) 137.
[32] J. Jakutis, N.U. Wetter, in: M.A.R.C. Alencar, L.R.P. Kassab, R.A. Kobayashi (Eds.), Advanced Solid-State Photonics 2006, WB23, The Optical Society of America, Washington, DC, 2006.
[33] D.L. Dexter, J. Chem. Phys. 21 (1953) 836.
[34] L.A. Riseberg, H.W. Moos, Phys. Rev. 174 (1968) 429.
[35] R. Reisfeld, Y. Eckstein, J. Chem. Phys. 63 (1975) 4001.
[36] R. Reisfeld, C. K. J Rgensen, Lasers and Excited States of Rare-Earth, Springer-Verlag, Berlin, Heidelberg, New York, 1977.
[37] X. Zou, H. Toratani, Phys. Rev. B52 (1995) 15889.
[38] J.Y. Allain, M. Monerie, H. Poignant, Electron. Lett. 28 (1992) 988.
[39] M. Weber, J. Lynch, D. Blackburn, D. Cronin, IEEE J. Quantum Electron. 19 (1983) 1600.
[40] E. Desurvier, Erbium-Doped Fibre Amplifiers—Principles and Applications, Wiley Interscience, New York, 2002, 218–219, 244–245.
[41] Animesh Jha, Purushottam Joshi, Shaoxiong Shen, Opt. Expr. 16 (2008) 13526.
[42] M. Pollnau, D.R. Gamelin, S.R. Lüthi, H.U. Güdel, M.P. Hehlen, Phys. Rev. B 61 (2000) 3337.
[43] X. Qiao, X. Fan, M. Wang, X. Zhang, J. Phys. D: Appl. Phys. 42 (2009) 055103.